Sensors and Materials, Vol. 37, No. 2 (2025) 607–616
MYU Tokyo

S & M 3941

$Tl_2NaScCl_6$: A New Tl-based Elpasolite Crystalline Scintillator

Miyu Ishida,* Akito Watanabe, Hiroki Kawamoto, Yutaka Fujimoto, and Keisuke Asai

Department of Applied Chemistry, Graduate School of Engineering, Tohoku University,
6-6-07 Aoba, Aramaki, Aoba-ku, Sendai 980-8579, Japan

(Received November 14, 2024; accepted January 8, 2025)

Keywords: scintillator, crystal, elpasolite, Tl, halide

A scintillator for X-ray and gamma-ray detection must possess high light yield, good energy resolution, and high effective atomic number. In this study, we fabricated $Tl_2NaScCl_6$ crystals using the vertical Bridgman method and investigated their luminescence, scintillation properties, and scintillation mechanisms. The photoluminescence and X-ray-induced radioluminescence (XRL) spectra reveal broad emission bands peaking at 410 and 430 nm, respectively. The temperature dependence of the intensity of XRL spectra follows the Arrhenius equation, indicating that the luminescence of the $Tl_2NaScCl_6$ crystals is a self-trapped exciton emission or exciton-related emission. The light yield and energy resolution calculated from the ^{137}Cs-gamma-ray pulse-height spectra are 20000 photons/MeV and 5.3%, respectively. These results suggest that $Tl_2NaScCl_6$ crystals are promising scintillators for X- and gamma-ray detection.

1. Introduction

Scintillators are phosphors that emit ultraviolet or visible light when exposed to high-energy photons and particles. The emitted light is converted into electrical signals using a photomultiplier tube (PMT). Devices that combine a scintillator and PMT are called scintillation detectors and are used to detect ionizing radiation. Scintillation detectors for X-rays and gamma rays are widely used in diagnostic imaging,[1] security inspection systems,[2] astrophysics research,[3] and high-energy physics experiments.[4] An ideal scintillator for X-ray and gamma-ray detection must possess high light yield, good energy resolution, high effective atomic number (Z_{eff}), and fast scintillation decay. Unfortunately, such a scintillator is yet to be discovered; therefore, novel materials must be developed.

Inorganic halide crystals are scintillator candidates for X- and gamma-ray detection. Halide scintillators have a narrower bandgap than oxide scintillators,[5] which leads to higher light yields according to the conventional Robbins model.[6] Therefore, various halide scintillators have been developed to obtain high light yield. Efficient self-trapped exciton (STE) emission has been observed in novel alkali halides and other ionic halide crystals (e.g., $Cs_5Cu_3Cl_6I_2$,[7] Rb_2CuBr_3,[8] $Cs_3Cu_2I_5$,[9] Rb_2AgCl_3,[10] and Cs_2ZrCl_6[11]). Exciton-related emissions generally include the recombination of a free exciton, which is a quasi-particle that forms when an electron and a hole become bound together owing to electrostatic attraction, without being confined to

*Corresponding author: e-mail: miyu.ishida.q8@dc.tohoku.ac.jp
https://doi.org/10.18494/SAM5482

ISSN 0914-4935
https://myukk.org/

any specific site or defect in a material. However, significant coupling between free excitons and lattices generates lattice distortion, resulting in STE emission.[12] Furthermore, in the case of STE emission, the self-trapped holes are stable and remain localized at low temperatures, which has produced high light yield in scintillators such as $Cs_3Cu_2I_5$,[9] Rb_2AgCl_3,[10] CsI,[13] and NaI.[14]

Crystalline scintillators with the elpasolite structure ($A^+_2B^+M^{3+}X^-_6$) are promising because of their high light yield and good energy resolution. The elpasolite structure is derived from the corresponding perovskite by cationic ordering. A strong rigid bond links the octahedra BX_6 and MX_6 to each other by common X atoms located at the octahedral vertices.[15] As cerium-based elpasolite crystalline scintillators, $Rb_2LiCeBr_6$ (light yield = 33000 photons/MeV, energy resolution = 6.3%, and Z_{eff} = 42.6);[16] $Cs_2NaCeBr_6$ (light yield = 25000 photons/MeV, energy resolution = 6.7%, and Z_{eff} = 47.8);[17] $K_2LiCeCl_6$ (light yield = 21000 photons/MeV, energy resolution = 16%, and Z_{eff} = 43.8);[18] and $Cs_2NaCeCl_6$ (light yield = 20000 photons/MeV, energy resolution = 8.3%, and Z_{eff} = 46.1)[19] have been reported to exhibit efficient luminescence without extrinsic dopant ions. Although these elpasolite crystals demonstrated good light yield and energy resolution, their Z_{eff} values are lower than those of commercial scintillators such as Gd_2SiO_5:Ce (Z_{eff} = 59.4),[20] Lu_2SiO_5:Ce (Z_{eff} = 65.4),[21] and $Bi_4Ge_3O_{12}$ (Z_{eff} = 75.2).[22]

In this study, we focused on thallium (Tl)-based elpasolite crystalline scintillators that have high Z_{eff} owing to the large atomic number of Tl (= 81). So far, high light yield with good energy resolutions and high Z_{eff} have been achieved using Tl-based elpasolite crystalline scintillators, such as Tl_2NaYCl_6 (light yield = 23000 photons/MeV, energy resolution = 6.3%, and Z_{eff} = 70.2)[23] and $Tl_2LiScCl_6$ (light yield = 26000 photons/MeV, energy resolution = 8.3%, and Z_{eff} = 67).[24] However, these scintillators and their emission mechanism remain understudied. In this study, we developed a $Tl_2NaScCl_6$ crystal as a new Tl-based elpasolite scintillator and investigated its luminescence and scintillation properties and scintillation mechanism.

2. Experimental Procedure

$Tl_2NaScCl_6$ crystal samples were prepared using the vertical Bridgman method in a two-zone furnace. The crystals were grown from TlCl (99.9%, Mitsuwa Chemicals Co., Ltd.); NaCl (99.999%, Sigma-Aldrich); and $ScCl_3{\cdot}6H_2O$ (99.9%, Mitsuwa Chemicals Co., Ltd.) powders. The powders were mixed in a TlCl:NaCl:$ScCl_3$ molar ratio of 2:1:1 and loaded into quartz ampoules, that were vacuum-sealed and then heated at 523 K under vacuum for 6 h to remove water. Subsequently, the ampoules were placed in the vertical Bridgman furnace. The temperatures of the upper and lower zones in the vertical furnace were 1323 and 1123 K, respectively. Crystal growth proceeded at a rate of 2.0 mm/h and a temperature gradient of 1.3 K/mm. After the growth, a fragment of the $Tl_2NaScCl_6$ crystal was cut, polished, and used for photoluminescence and scintillation measurements. Other parts of the $Tl_2NaScCl_6$ crystal were used to measure powder X-ray diffraction (XRD) patterns at room temperature.

A Rigaku Ultima IV diffractometer with CuK_α radiation was used to measure XRD patterns. A fluorescence spectrophotometer (Hitachi High-Tech F-7000) equipped with a Xe lamp was used to measure the excitation and photoluminescence (PL) spectra at room temperature. A

fluorescence lifetime spectrofluorometer (Horiba, DeltaFlex 3000U-TMK2) with an LED (Horiba, NanoLED-250) as the excitation source was used to obtain PL decay time profiles at room temperature. An X-ray generator (Rigaku, D2300-HK) operating at 40 mA and 40 kV with a Cu-K_α target as the excitation source was used to measure X-ray-excited radioluminescence (XRL) spectra. The spectra were recorded using a QE Pro spectrometer (Ocean Insight). To measure the temperature dependence of the XRL spectra, the samples were cooled in a cryostat from 300 to 10.5 K under vacuum, and the XRL spectra were measured at 25 K intervals. Our original setup[25] developed using the delayed coincidence method[26] was employed to measure the scintillation decay time profiles, in which sealed ^{22}Na was used as the gamma-ray radiation source. A combination of a pilot-U plastic scintillator and a PMT (Hamamatsu Photonics, H3378-51) was used to generate the trigger signal for the measurement. Scintillation photons from the samples were detected using a PMT (Hamamatsu Photonics, R7400P), which provided the stop pulse. Our original setup[25] was also used to measure the ^{137}Cs-gamma-ray pulse-height spectra. The spectrum of the $Tl_2NaScCl_6$ crystal was recorded with a shaping time of 10 μs. The commercially available scintillator Gd_2SiO_5:Ce (GSO) was used as a reference sample.

3. Results and Discussion

3.1 Grown crystal sample and XRD analysis

Figure 1 shows a polished $Tl_2NaScCl_6$ crystal. The sample is translucent and colorless. The $Tl_2NaScCl_6$ crystal was slightly hygroscopic, similar to other elpasolite crystals such as $Cs_2LiCeBr_6$[27] and Cs_2LiYCl_6.[28] To avoid exposing the crystal surface to air, the $Tl_2NaScCl_6$ crystal was covered with optical grease for luminescence and scintillation measurements. Figure 2 shows the XRD patterns of the $Tl_2NaScCl_6$ crystal. No data on $Tl_2NaScCl_6$ crystals are available in the Inorganic Crystal Structure Database. Therefore, the data for $Tl_2NaScCl_6$ elpasolite crystal in the Springer Materials online database (sd_1715000) were selected as the reference. From the result, all the peaks of the grown crystal were found to match those of the reference data. This result indicates that $Tl_2NaScCl_6$ has an elpasolite-type crystal structure.

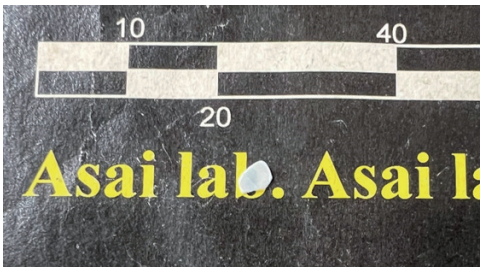

Fig. 1. (Color online) Photograph of the polished $Tl_2NaScCl_6$ crystal next to a mm-scale bar.

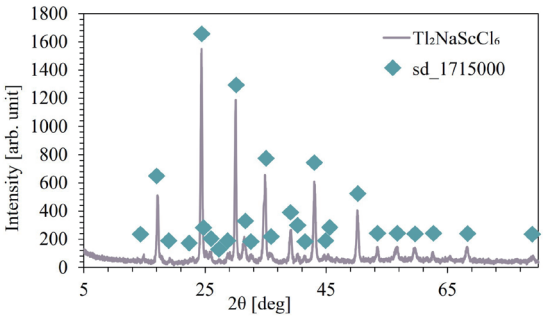

Fig. 2. (Color online) XRD patterns of $Tl_2NaScCl_6$ crystal.

3.2 PL properties

Figure 3 shows the excitation and PL spectra of the $Tl_2NaScCl_6$ crystal. The excitation spectrum, monitored at an emission wavelength of 410 nm, shows peaks at around 200, 240, and 280 nm. These excitation bands are attributed to the C, B, and A bands, respectively. The C band ($^1S_0 \rightarrow {}^1P_1$) transition is dipole-allowed. The B band ($^1S_0 \rightarrow {}^3P_2$) transition is partially allowed owing to noncubic phonons. The A band ($^1S_0 \rightarrow {}^3P_1$) transition is spin-forbidden, but is allowed owing to the spin–orbit interaction between the $^3P_1$ and $^1P_1$ states.[29,30] An emission band is observed at 410 nm under 240 nm excitation. A similar band was previously reported for the Tl_2NaYCl_6 crystal.[23] The Stokes shift and full width at half-maximum (FWHM) of $Tl_2NaScCl_6$ were estimated to be approximately 11000 cm^{-1} and 80 nm, respectively. Crystals showing STE emission indicate large Stokes shifts (e.g., Cs_4SnBr_6: 10000 cm^{-1};[31] $Cs_3Cu_2I_3Br_2$: 12000 cm^{-1}; and $Cs_3Cu_2I_5$: 13000 cm^{-1}[32]). From the large Stokes shift and broad emission band of the $Tl_2NaScCl_6$ crystal, the origin of the emission is plausibly STE recombination.

Figure 4 shows the PL decay time profiles of the $Tl_2NaScCl_6$ crystal with excitation and emission wavelengths of 255 nm and 415 nm, respectively. The PL decay curves were fitted using three exponential decay functions. The calculated decay time constants are 6 ns (27%), 33 ns (50%), and 264 ns (23%). The percentages in parentheses show the contribution of each PL decay time constant to the emission of the $Tl_2NaScCl_6$ crystal. In a previous study using the same measurement instrument,[23] a decay time constant of 6 ns was related to the detection of scattered excitation photons. The decay time constants of 33 and 264 ns are comparable to those of the Tl_2NaYCl_6 (58 and 680 ns)[23] and Tl_2LiYCl_6 (13 and 410 ns)[33] crystals. According to the traditional understanding of the STE emission process in alkali halides,[34] STEs undergo a radiative or nonradiative decay from local minima on the adiabatic potential energy surfaces (APESs) of the lowest singlet and triplet states. Furthermore, the properties of APESs, such as their shape and the presence of multiple minima, are affected by the host crystals and molecule–ion X^{2-} translation (configuration coordinate Q_2). The combination of the spin multiplicity and the stability of these APESs gives rise to various features of STE emission. Thus, the two components of the decay time are possibly attributable to the transitions from singlet and triplet states affected by the host crystals and molecule–ion X^{2-} translation. The above-mentioned decay time constants of other Tl-based elpasolite crystals also support the hypothesis that the emission in the PL spectrum of the $Tl_2NaScCl_6$ crystal originates from STE recombination.

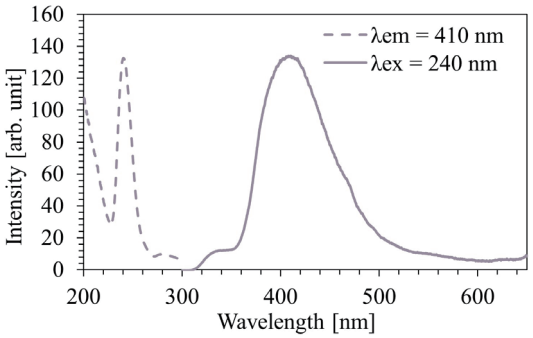

Fig. 3. (Color online) Excitation (dashed line) and PL (solid line) spectra of $Tl_2NaScCl_6$ crystal.

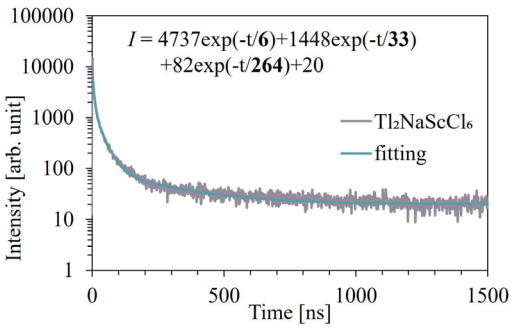

Fig. 4. (Color online) PL decay time profiles of $Tl_2NaScCl_6$ crystal (λ_{ex} = 255 nm, λ_{em} = 415 nm). The light blue line is a fit with the exponential functions.

3.3 Scintillation properties

Figure 5 shows the XRL spectrum of the $Tl_2NaScCl_6$ crystal. The emission wavelength shows a peak at 430 nm, which ideally matches the peak wavelength to achieve the wavelength-dependent sensitivities of conventional PMT. The XRL peak wavelength of the $Tl_2NaScCl_6$ crystal is similar to those of Tl_2NaYCl_6[23] and Tl_2LiYCl_6[33] crystals. The XRL spectrum does not include the emission peak associated with the s–p transitions of Tl^+, which has been reported for CsCl:Tl[35] and Cs_2CdCl_4:Tl[36] crystals, suggesting that the X-ray-induced scintillation originates from the recombination of STEs, similarly to PL.

Figure 6(a) shows the temperature dependence of the XRL spectrum of a $Tl_2NaScCl_6$ crystal at 50 K intervals. Figure 6(b) shows the temperature dependence of the XRL intensity of each dominant band and sub-band, and the integrated XRL intensity of both bands. The luminescence intensity of the dominant bands peaking at around 430 nm increases with temperature from 10.5 to 100 K, reaches a maximum at 100 K, and then decreases from 100 to 300 K. In addition, the peak wavelengths shift towards higher energies with increasing temperature in the range of 10.5–75 K. In the 10.5–75 K range, sub-bands peaking at around 660 nm are observed, whose luminescence intensity decreases with increasing temperature from 10.5 to 300 K. Therefore, at temperatures in the range of 10.5–75 K, the dominant bands and sub-bands correlate inversely with temperature. Here, the integrated XRL intensity decreases gradually with increasing temperature from 10.5 to 300 K, as shown in Fig. 6(b). Figure 7 shows the temperature

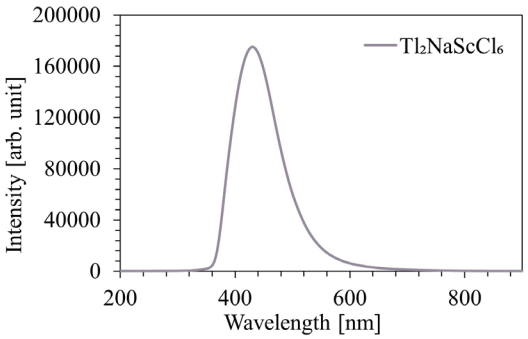

Fig. 5. (Color online) XRL spectrum of $Tl_2NaScCl_6$ crystal.

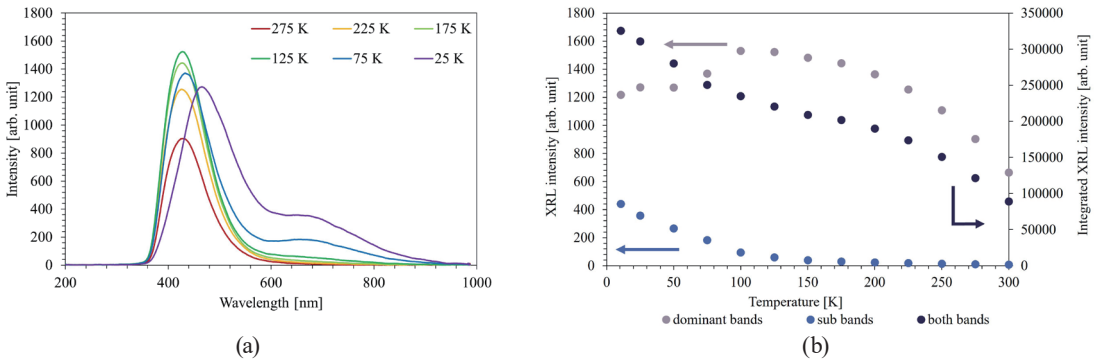

Fig. 6. (Color online) (a) Temperature dependence of the XRL spectrum of $Tl_2NaScCl_6$ crystal and (b) temperature dependence of the XRL intensity of each dominant band and sub-band, and the integrated XRL intensity of both bands.

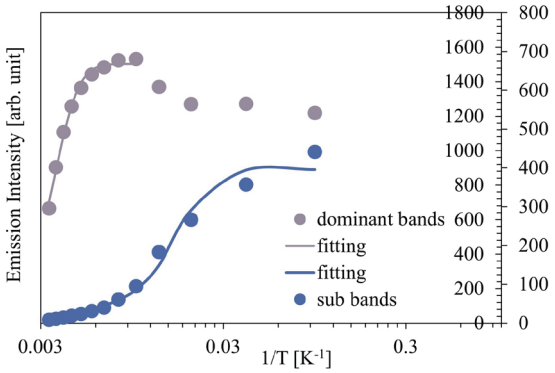

Fig. 7. (Color online) Temperature dependence of XRL intensity and data fitted using the modified Arrhenius function of both dominant bands peaking at around 430 nm and sub-bands peaking at around 660 nm.

dependence of the XRL intensity of both dominant bands peaking at approximately 430 nm and the sub-bands peaking at approximately 660 nm. If the luminescence of the dominant band originates from STE emission and exciton-related emission, it should follow the Arrhenius equation,[12] in which radiative transitions from one luminescent excited state compete with nonradiative transitions to another. Therefore, the Arrhenius equation describes the absolute temperature as

$$I(T) = \frac{I_0}{1 + \tau_R \nu_0 \exp(-E/kT)}, \tag{1}$$

where $I(T)$ is the total emission intensity, I_0 is the emission intensity in the absence of competition, τ_R is the constant radiative decay rate, ν_0 is the maximum rate of branching to a nonradiative de-excitation channel, E is the activation energy, k is the Boltzmann constant, and T is the absolute temperature. Equation (1) is derived using Eqs. (2) and (3) as below:[12]

$$\tau(T) = \left[(\tau_R)^{-1} + \nu_0 \exp(-E/kT) \right]^{-1}, \tag{2}$$

$$I(T) = \frac{I_0 \tau(T)}{\tau_R}, \tag{3}$$

where $\tau(T)$ is the temperature-dependent lifetime of luminescence. Since in the case of this experiment, relative light yields can be proportional to XRL intensities, we replaced the total light yield [= $I(T)$] and light yield in the absence of competition (= I_0) with the total emission intensity and emission intensity in the absence of competition, respectively.

The dominant bands were fitted in the region 100–300 K, where the emission intensity decreases monotonically with increasing temperature. Both the dominant bands and sub-bands were well fitted using Eq. (1) in the above range. Therefore, from the temperature dependence and PL measurements, the dominant band luminescence can be attributed to STE emission. In this case, the activation energies were calculated to be around 140 meV for the dominant bands and around 20 meV for the sub-bands. The deviation of the dominant band behavior from the

Arrhenius equation below 75 K is possibly affected by the sub-band, which correlates inversely with temperature. Studying the origin of the sub-band is beyond the scope of this study; however, we speculate that it is a crystalline-defect-induced emission.

Figure 8 shows the scintillation decay time profiles of the $Tl_2NaScCl_6$ crystal. The scintillation decay curves were fitted using two exponential decay functions, producing decay time constants of 181 ns (63%) and 906 ns (37%). From the comparison with the decay time constants under UV light excitation, it can be confirmed that the scintillation decay is slow. This significant difference between decay time constants could be attributed to differences in the energy migration processes. The PL exhibited features characteristic of localized emission centers, indicating that only these centers were involved in the excitation and relaxation processes. On the other hand, in scintillation, the transport of secondary electrons to the emission centers plays an important role in the characterizations, in addition to the localized emission centers. In the case of the $Tl_2NaScCl_6$ crystal, it is considered that the transport process, which strongly depends on the trap levels of electrons and holes, caused the delay of scintillation decay. The same functions were used for the Tl_2NaYCl_6 crystal, producing the respective time constants of 350 and 2500 ns.[23] In addition, the decay time constants of the $Tl_2NaScCl_6$ crystal are similar to those of other thallium-based chloride crystal scintillators, such as Tl_2ZnCl_4 (122 and 827 ns).[37] The emission in the Tl_2ZnCl_4 crystal[37] is attributed to STE emission. This report supports the hypothesis that the origin of the emission in the XRL spectra of the $Tl_2NaScCl_6$ crystal is STE recombination.

Figure 9 shows the ^{137}Cs-gamma-ray pulse-height spectra of the $Tl_2NaScCl_6$ and GSO crystals. The light yield of the GSO crystal used as a reference is 10000 photons/MeV. For the $Tl_2NaScCl_6$ crystal, two peaks are observed at channels 550 and 630. The former peak corresponds to the escape of K_α X-rays from Tl atoms of the crystal, and the latter peak corresponds to photoabsorption. The photoabsorption peak of the GSO crystal is observed at channel 600. The PMT quantum efficiencies are 39% and 38% for the $Tl_2NaScCl_6$ and GSO crystals, respectively. The light yield calculated for the $Tl_2NaScCl_6$ crystal on the basis of the photoabsorption peak channels and PMT quantum efficiencies is 20000 photons/MeV. The energy resolutions estimated using Gaussian fitting are 5.3 and 8.7% for the $Tl_2NaScCl_6$ and GSO crystals, respectively. Therefore, the light yield and energy resolution of the $Tl_2NaScCl_6$ crystal are superior to those of commercially available GSO crystal scintillators.

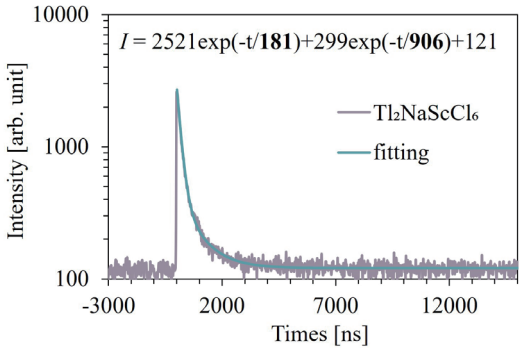

Fig. 8. (Color online) Scintillation decay time profiles of the $Tl_2NaScCl_6$ crystal. The light blue line is a fit obtained using the exponential functions.

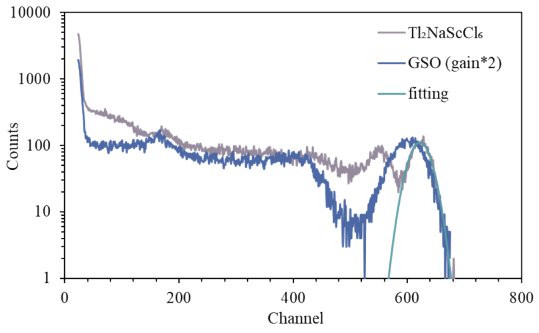

Fig. 9. (Color online) ^{137}Cs-gamma-ray pulse-height spectra of the $Tl_2NaScCl_6$ and GSO crystals. The light blue line is a fit.

Table 1
Physical and scintillation properties of Tl-based halide crystalline scintillators.

Compound	Z_{eff}	Emission peak wavelength (nm)	Light yield (photons/MeV)	Energy resolution (%)	Reference
$Tl_2NaScCl_6$	71.1	430	20000	5.3	This study
Tl_2NaYCl_6	70.2	430	23000	6.3	23
$Tl_2LiScCl_6$	67	385	26000	8.3	24
$TlMgCl_3$	71.6	405	46000	5.0	38
	70	409	30600	3.7	39
Tl_2HfCl_6	72.7	450	24200	17.7	40
	72	398	32000	4.0	41
Tl_2ZrCl_6	70.7	470	50800	5.6	40
	69	460	47000	4.3	42
$TlCaCl_3$	65.5	425	30600	5.0	43
$TlSr_2Cl_5$	63.7	430 and 490	19000	N. D.	44
Tl_2GdCl_5	71	390	9300	15	45
$TlGd_2Cl_7$	64	350–550	1700	20	46
Tl_2LaCl_5	70	355	31500	7.2	47
$TlCdCl_3$	68.7	450	2200	N. D.	48
Tl_2ZnCl_4	73.2	490	10000	N. D.	37

3.4 Discussion

Table 1 lists the physical and scintillation properties of the Tl-based halide crystalline scintillators. The Z_{eff} of the $Tl_2NaScCl_6$ crystal is similar to those of other Tl-based halide crystals. The $Tl_2NaScCl_6$ crystal has the highest Z_{eff} among Tl-based elpasolite crystals. The scintillation emission peak wavelength of the $Tl_2NaScCl_6$ crystal is 430 nm, which is similar to those of the Tl_2NaYCl_6, $TlCaCl_3$, and $TlSr_2Cl_5$ crystals. The light yield of the $Tl_2NaScCl_6$ crystal is similar to those of other Tl-based elpasolite crystals and higher than those of the $TlSr_2Cl_5$, Tl_2GdCl_5, $TlGd_2Cl_7$, $TlCdCl_3$, and Tl_2ZnCl_4 crystals. The energy resolution of the $Tl_2NaScCl_6$ crystal is the smallest among Tl-based elpasolite crystals and similar to those of the $TlMgCl_3$, Tl_2ZrCl_6, and $TlCaCl_3$ crystals.

4. Conclusions

A $Tl_2NaScCl_6$ crystal was fabricated, and its luminescence, scintillation properties, and scintillation mechanism were investigated. $Tl_2NaScCl_6$ crystal samples were prepared using the vertical Bridgman method in a two-zone furnace. A broad emission band peaking at 430 nm was observed in the XRL spectrum. The temperature-dependent XRL spectra showed a luminescence peak at around 430 nm, which increased with temperature from 10.5 to 100 K, reached a maximum at 100 K, then decreased from 100 to 300 K. In the range of 100–300 K, the temperature dependence of XRL intensity followed the Arrhenius equation. Therefore, the origin of the luminescence of the $Tl_2NaScCl_6$ crystal is concluded to be STE emission or exciton-related emission. The decay time constants calculated from the scintillation decay time profiles were 181 and 906 ns. The light yield and energy resolution calculated from the ^{137}Cs-gamma-ray pulse-height spectra were 20000 photons/MeV and 5.3%, respectively. The Z_{eff} and energy resolution of the $Tl_2NaScCl_6$ crystal respectively were the highest and smallest among Tl-based elpasolite crystals.

Acknowledgments

This study was supported by a Grant-in-Aid for Scientific Research (A) (Grant No. 22H00308, 2022–2026) and a Grant-in-Aid for Challenging Research (Exploratory) (Grant No. 24K21544, 2024–2026) funded by the Japan Society for the Promotion of Science, a 2024 research grant from Amano Institute of Technology, a 2023 research grant from the Research Foundation for the Electrotechnology of Chubu, a matching fund between National Institute of Advanced Industrial Science and Technology (AIST) and Tohoku University, the Cooperative Research Program of "Network Joint Research Center for Materials and Devices (MEXT), and a 2024 research grant from Iketani Science and Technology Foundation.

References

1 D. Pacella: Rep. Med. Imag. **8** (2015) 1. https://doi.org/10.2147/RMI.S50045
2 D. Totsuka, T. Yanagida, K. Fukuda, N. Kawaguchi, Y. Fujimoto, J. Pejchal, Y. Yokota, and A. Yoshikawa: Nucl. Instrum. Meth. Phys. Res. **659** (2011) 399. https://doi.org/10.1016/j.nima.2011.08.014
3 T. Itoh, M. Kokubun, T. Takashima, T. Honda, K. Makishima, T. Tanaka, T. Yanagida, S. Hirakuri, R. Miyawaki, H. Takahashi, K. Nakazawa, and T. Takahashi: IEEE Trans. Nucl. Sci. **53** (2006) 2983. https://doi.org/10.1109/TNS.2006.879760
4 T. Ito and T. Yamaguchi: J. Photopolym. Sci. Technol. **20** (2007) 239. https://doi.org/10.2494/photopolymer.20.239
5 P. Dorenbos: IEEE Trans. Nucl. Sci. **57** (2010) 1162. https://doi.org/10.1109/TNS.2009.2031140
6 D. J. Robbins: J. Electrochem. Soc. **127** (1980) 2694. https://doi.org/10.1149/1.2129574
7 X. Niu, J. Xiao, B. Lou, Z. Yan, Q. Zhou, T. Lin, C. Ma, and X. Han: Ceram. Int. **48** (2022) 30788. https://doi.org/10.1016/j.ceramint.2022.07.032
8 B. Yang, L. Yin, G. Niu, J. Yuan, K. Xue, Z. Tan, X. Miao, M. Niu, X. Du, H. Song, E. Lifshitz, and J. Tang: Adv. Mater. **31** (2019) 1904711. https://doi.org/10.1002/adma.201904711
9 D. Yuan: ACS Appl. Mater. Interfaces **12** (2020) 38333. https://doi.org/10.1021/acsami.0c09047
10 Z. Zhang, X. Guo, K. Huang, X. Sun, X. Li, H. Zeng, X. Zhu, Y. Zhang, and R. Xie: J. Lumin. **241** (2022) 118500. https://doi.org/10.1016/j.jlumin.2021.118500
11 K. Saeki, Y. Fujimoto, M. Koshimizu, T. Yanagida, and K. Asai: Appl. Phys. Express. **9** (2016) 042602. https://doi.org/10.7567/APEX.9.042602
12 R. T. Williams and K. S. Song: J. Phys. Chem. Solids. **51** (1990) 679. https://doi.org/10.1016/0022-3697(90)90144-5
13 M. Moszynski, M. Balcerzyk, W. Czarnacki, M. Kapusta, W. Klamra, P. Schotanus, A. Syntfeld, M. Szawlowski, and V. Kozlov: Nucl. Instrum. Methods Phys. Res., Sect. A **537** (2005) 357. https://doi.org/10.1016/j.nima.2004.08.043
14 P. Sibczynski, M. Moszynski, T. Szczesniak, and W. Czarnacki: J. Inst. **7** (2012) 11006. https://doi.org/10.1088/1748-0221/7/11/P11006
15 I.N. Flerov, M.V. Gorev, K.S. Aleksandrow, A. Tressaud, J. Grannec, and M. Couzi: Mater. Sci. Eng. **24** (1998) 81. https://doi.org/10.1016/S0927-796X(98)00015-1
16 G. Rooh, H. J. Kim, H. Park, and S. Kim: IEEE Trans. Nucl. Sci. **57** (2010) 3836. https://doi.org/10.1109/TNS.2010.2079949
17 S. Kim, G. Rooh, H. J. Kim, W. Kim, and U. Hong: IEEE Trans. Nucl. Sci. **57** (2010) 1251. https://doi.org/10.1109/TNS.2010.2041789
18 J. Y. Cho, H. J. Kim, A. Khan, and J. M. Park: Radiat. Meas. **141** (2021) 106524. https://doi.org/10.1016/j.radmeas.2021.106524
19 G. Rooh, H. Kang, H. J. Kim, H. Park, and S. Kim: J. Cryst. Growth. **311** (2009) 2470. https://doi.org/ https://doi.org/10.1016/j.jcrysgro.2009.01.091
20 K. Takagi and T. Fukazawa: Appl. Phys. Lett. **42** (1983) 43. https://doi.org/10.1063/1.93760
21 C. L. Melcher and J. S. Schweitzer: IEEE Trans. Nucl. Sci. **39** (1992) 502. https://doi.org/10.1109/23.159655
22 M. J. Weber and R. R. Monchamp: J. Appl. Phys. **44** (1973) 5495. https://doi.org/10.1063/1.1662183
23 M. Arai, K. Mizoi, Y. Fujimoto, M. Koshimizu, D. Nakauchi, T. Yanagida, and K. Asai: J. Mater. Sci. **32** (2021) 7906. https://doi.org/10.1007/s10854-021-05514-4

24 M. Kim, H. J. Kim, J. Y. Cho, A. Khan, D. J. Daniel, and G. Rooh: J. Korean Phys. Soc. **76** (2020) 706. https://doi.org/10.3938/jkps.76.706
25 A. Sato, A. Magi, M. Koshimizu, Y. Fujimoto, S. Kishimoto, and K. Asai: RSC Adv. **11** (2021) 15581. https://doi.org/10.1039/d1ra01878g
26 L. M. Bollinger and G. E. Thomas: Rev. Sci. Instrum. **32** (1961) 1044. https://doi.org/10.1063/1.1717610
27 J. K. Cheon, S. Kim, G. Rooh, J. H. So, H. J. Kim, and H. Park: Nucl. Instrum. Methods Phys. Res., Sect. A **652** (2011) 205. https://doi.org/10.1016/j.nima.2011.02.038
28 J. Glodo, R. Hawrami, and K. S. Shah: J. Cryst. Growth **379** (2013) 73. https://doi.org/10.1016/j.jcrysgro.2013.03.023
29 K. Kubota and T. Kawai: J. Phys. Chem. Solids **163** (2022) 110592. https://doi.org/10.1016/j.jpcs.2022.110592
30 D. J. Daniel, I. R. Pandey, H. J. Kim, M. H. Lee, and M. Tyagi: J. Lumin. **223** (2020) 117197. https://doi.org/10.1016/j.jlumin.2020.117197
31 B. M. Benin, D. N. Dirin, V. Morad, M. Worle, S. Yakunin, G. Raino, O. Nazarenko, M. Fischer, I. Infante, and M. V. Kovalenko: Angrew. Chem. Int. Ed. **57** (2018) 11329. https://doi.org/10.1002/anie.201806452
32 T. Haposan, A. Arramel, P. Y. D. Maulida, S. Hartati, A. A. Afkauni, M. H. Mahyuddin, L. Zhang, D. Kowal, M. E. Witkowski, K. J. Drozdowski, M. Makowski, W. Drozdowski, L. J. Diguna, and M. D. Birowosuto: J. Mater. Chem. C **12** (2024) 2398. https://doi.org/10.1039/D3TC03977C
33 F. Moretti, D. Onken, D. Perrodin, and E. Bourret: J. Lumin. **241** (2022) 118549. https://doi.org/10.1016/j.jlumin.2021.118549
34 K. S. Song and R. T. Williams: Self-Trapped Excitons (Springer, 1995) Chap. 5, p. 123.
35 T. Sakai, M. Koshimizu, Y. Fujimoto, D. Nakauchi, T. Yanagida, and K. Asai: Jpn. J. Appl. Phys. **56** (2017) 062601. https://doi.org/10.7567/JJAP.56.062601
36 T. Sakai, M. Koshimizu, Y. Fujimoto, D. Nakauchi, T. Yanagida, and K. Asai: Sens. Mater. **30** (2018) 1564. https://doi.org/10.18494/SAM.2018.1920
37 M. Arai, Y. Fujimoto, M. Koshimizu, D. Nakauchi, T. Yanagida, and K. Asai: Opt. Mater. **109** (2020) 110455. https://doi.org/10.1016/j.optmat.2020.110455
38 Y. Fujimoto, M. Koshimizu, T. Yanagida, G. Okada, K. Saeki, and K. Asai: Jpn. J. Appl. Phys. **55** (2016) 090301. https://doi.org/10.7567/JJAP.55.090301
39 R. Hawrami, E. Ariesanti, H. Wei, J. Finkelstein, J. Glodo, and K. S. Shah: J. Cryst. Growth **475** (2017) 216. https://doi.org/10.1016/j.jcrysgro.2017.06.012
40 Y. Fujimoto, K. Saeki, D. Nakauchi, T. Yanagida, M. Koshimizu, and K. Asai: Sens. Mater. **30** (2018) 1577. https://doi.org/10.18494/SAM.2018.1927
41 P. Q. Vuong, M. Tyagi, S. H. Kim, and H. J. Kim: CrystEngComm. **21** (2019) 5898. https://doi.org/10.1039/C9CE01202H
42 Q. V. Phan, H. J. Kim, G. Rooh, and S. H. Kim: J. Alloys Compd. **766** (2018) 326. https://doi.org/10.1016/j.jallcom.2018.06.349
43 A. Khan, G. Rooh, H. J. Kim, H. Park, and S. Kim: Radiat. Meas. **107** (2017) 115. https://doi.org/10.1016/j.radmeas.2017.09.003
44 M. Arai, K. Takahashi, Y. Fujimoto, M. Koshimizu, T. Yanagida, and K. Asai: Radiat. Meas. **134** (2020) 106328. https://doi.org/10.1016/j.radmeas.2020.106328
45 G. Rooh, A. Khan, H. J. Kim, H. Park, and S. Kim: IEEE Trans. Nucl. Sci. **65** (2018) 2157. https://doi.org/10.1109/TNS.2018.2822339
46 A. Khan, G. Rooh, H. J. Kim, and S. Kim: IEEE Trans. Nucl. Sci. **65** (2018) 2152. https://doi.org/10.1109/TNS.2018.2829198
47 U. Shirwadkar, M. Loyd, M. Du, E. Loef, G. Ciampi, L. S. Pandian, L. Stand, M. Koschan, M. Zhuravleva, C. Melcher, and K. Shah: Nucl. Instrum. Methods Phys. Res., Sect. A **962** (2020) 163684. https://doi.org/10.1016/j.nima.2020.163684
48 Y. Fujimoto, K. Saeki, T. Yanagida, M. Koshimizu, and K. Asai: Radiat. Meas. **106** (2017) 151. https://doi.org/10.1016/j.radmeas.2017.03.034